Article

Controlled Magnetic Anisotropy in Single Domain Mn-doped Biosynthesized Nanoparticles

Lourdes Marcano,* Iñaki Orue, Ana García-Prieto, Radu Abrudan, Javier Alonso, Luis Fernández Barquín, Sergio Valencia, Alicia Muela, and M. Luisa Fdez-Gubieda

Cite This: *J. Phys. Chem. C* 2020, 124, 22827−22838

Read Online

ACCESS | Metrics & More | Article Recommendations | SI Supporting Information

ABSTRACT: Magnetotactic bacteria *Magnetospirillum gryphiswaldense* synthesize cubo-octahedral shaped magnetite nanoparticles, called magnetosomes, with a mean diameter of 40 nm. The high quality of the biosynthesized nanoparticles makes them suitable for numerous applications in fields like cancer therapy, among others. The magnetic properties of magnetite magnetosomes can be tailored by doping them with transition metal elements, increasing their potential applications. In this work, we address the effect of Mn doping on the main properties of magnetosomes by the combination of structural and magnetic characterization techniques. Energy-dispersive X-ray spectroscopy, X-ray absorption near-edge structure, and X-ray magnetic circular dichroism results reveal a Mn dopant percentage of utmost 2.3%, where Mn cations are incorporated as a combination of Mn^{2+} and Mn^{3+}, preferably occupying tetrahedral and octahedral sites, respectively. Fe substitution by Mn notably alters the magnetic behavior of the doped magnetosomes. Theoretical modeling of the experimental hysteresis loops taken between 5 and 300 K with a modified Stoner–Wohlfarth approach highlights the different anisotropy contributions of the doped magnetosomes as a function of temperature. In comparison with the undoped magnetosomes, Mn incorporation alters the magnetocrystalline anisotropy introducing a negative and larger cubic anisotropy down to the Verwey transition, which appears shifted to lower temperature values as a consequence of Mn doping. On the other hand, Mn-doped magnetosomes show a decrease in the uniaxial anisotropy in the whole temperature range, most likely associated with a morphological modification of the Mn-doped magnetosomes.
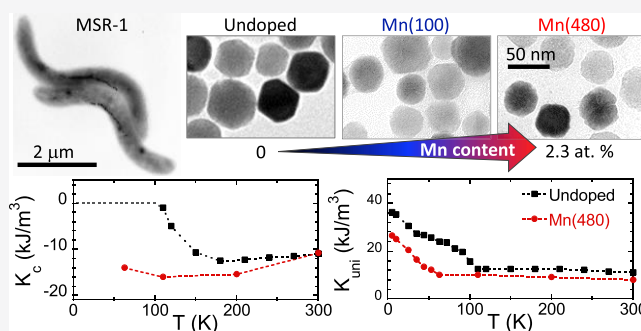
INTRODUCTION

Magnetotactic bacteria are a group of aquatic microorganisms widespread in freshwater and marine environments that can passively align in the presence of magnetic fields while they actively swim. This fascinating behavior is due to the presence of intracellular membrane-enclosed single domain magnetic nanoparticles, called magnetosomes, arranged in chains.[1−4] Magnetosomes present a species-specific morphology and size, and a precise mineral composition, in most cases magnetite. The biological precision exhibited in the synthesis process bestows exceptional properties on magnetosomes, which attracts a lot of scientific attention, being excellent candidates for biomedical applications.[5−9] In addition, recent studies have addressed the possibility of exploiting the whole magnetotactic bacteria as microrobots for cancer treatment.[10−12] These microorganisms provide a self-propelling mechanism secured by their flagella and the advantage to be manipulated and guided, thanks to the presence of the magnetosome chain. Furthermore, the biological structure of the magnetosome chain of magnetotactic bacteria enhances the hyperthermia efficiency compared with isolated magnetosomes and their synthetic counterparts.[13]

Aiming to expand the range of applications of magnetosomes and magnetotactic bacteria, the past decade has witnessed a huge growth in the development of different strategies to tailor magnetosome properties, which are otherwise set by the genetic control of the bacteria. The substitution of iron cations by transition metal dopants in magnetite serves as a proven method to change the magnetic properties of the magnetic nanoparticles.[14] Under this premise, Staniland et al.[15] pioneered the in vivo Co doping of magnetosomes under laboratory conditions by simply adding certain amounts of this element into the culture medium.[15] Since then, several groups have been able to dope magnetosomes with different transition metals such as Co, Mn, and Cu.[16−22]

To this respect, doping the magnetosomes with Mn is especially attractive due to the higher magnetization with respect to magnetite, lower coercivity, and proven biocompatibility evidenced in synthetic Mn-substituted magnetite ($Mn_xFe_{3-x}O_4$) nanoparticles.[23−25] There are several reports in the literature addressing the incorporation of Mn into the inner structure of magnetosomes synthesized by different bacterial strains. Keim et al. first evidenced the presence of Mn accumulation in the magnetosomes synthesized by mixed populations of uncultured bacteria exposed to $MnCl_2$.[26] They detected up to 2.81 atomic % Mn by elemental analysis of thin sections of the synthesized magnetosomes. Later, Tanaka et al. analyzed the Mn doping of *Magnetospirillum magneticum* AMB-1 grown in a Mn-supplemented medium, reporting values of 2.7 atomic % Mn.[16] In the same way, Prozorov et al. and Pérez Gonzalez et al. presented a detailed characterization of magnetosomes in *Magnetospirillum gryphiswaldense* MSR-1 cells, grown in a Mn-containing medium, reaching values of 1 atomic % Mn cations.[20,21] These studies evidenced the tuning of the magnetic properties of the doped magnetosomes as a consequence of Mn incorporation by a reduction of the coercivity, an enhancement of the magnetic susceptibility, and a shift to lower temperatures of the Verwey transition, a fingerprint of magnetite. However, some key aspects as the oxidation state and coordination of the Mn in the doped magnetosomes and the origin of the resulting magnetic behavior still remain largely unknown.

In this study, we address the Mn doping of magnetosomes synthesized by *M. gryphiswaldense* MSR-1. *M. gryphiswaldense* forms cubo-octahedral magnetite nanoparticles with an average diameter of ≈40 nm and a narrow size distribution of ≈8 nm. By the combination of structural and magnetic characterization techniques such as transmission electron microscopy (TEM) with energy-dispersive X-ray spectroscopy (EDX), X-ray absorption near-edge structure (XANES), and X-ray magnetic circular dichroism (XMCD), we evidence the presence of Mn (up to 2.3 atomic %) in the magnetite structure. Our measurements suggest that Mn cations are incorporated as a combination of Mn^{2+} and Mn^{3+} preferably occupying tetrahedral and octahedral sites, respectively. The incorporation of Mn strongly influences the magnetic behavior of the synthesized magnetosomes. Theoretical modeling of the hysteresis loops of the Mn-doped magnetosome chains with a modified Stoner−Wohlfarth approach sheds light on the different anisotropy contributions and their temperature dependence.

■ EXPERIMENTAL SECTION

Bacterial Strain and Growth Conditions. *M. gryphiswaldense* MSR-1 (DMSZ 6631) was grown in a modified flask standard medium[27] in three-fourth 1 L-bottles loosely capped at 28 °C without shaking for 120 h, after which well-formed magnetosomes were observed. Prior to the inoculation, the growth medium was supplemented with different amounts of Fe and Mn as Fe(III) and Mn(II)-citrates, respectively. Three samples were produced: (i) undoped magnetosomes (100 μM Fe(III)-citrate), (ii) Mn(100) (10 μM Fe(III)-citrate and 100 μM Mn(II)-citrate), and (iii) Mn(480) magnetosomes (10 μM Fe(III)-citrate and 480 μM Mn(II)-citrate).

Magnetosomes have been measured either in the whole cells or isolated from the bacteria.

For the preparation of whole cell samples, the cells were harvested by centrifugation, fixed in 2% glutaraldehyde, and washed three times in mQ water and concentrated up to 10^8 cell/mL.

Complementarily, magnetosomes were isolated from the bacteria following the protocol described by Grünberg et al.[28] with minor modifications. The cells were collected by centrifugation, suspended in 20 mM HEPES-4 mM EDTA (pH = 7.4), and disrupted using a French press (P = 1.4 kbar). The lysated cells were sonicated to promote the separation of magnetosomes and centrifuged at 600 g for 5 min to remove cell debris. Then, magnetosomes were collected from the supernatant by magnetic separation and rinsed 10 times with 10 mM HEPES-200 mM NaCl (pH = 7.4). Finally, the isolated magnetosomes were redispersed in ultra-pure water.

Transmission Electron Microscopy (TEM), Energy-Dispersive X-ray Spectroscopy (EDX), and High-Resolution TEM (HRTEM). TEM images were obtained on unstained cells and isolated magnetosomes adsorbed onto 300 mesh carbon-coated Cu grids with a Philips CM200 electron microscope that includes an EDX detector at an accelerating voltage of 200 kV. The particle-size distribution of the isolated magnetosomes was analyzed using a standard software for digital electron microscope image processing, ImageJ.[29] EDX spectra were acquired with a counting time of 5 min to optimize the signal-to-noise ratio while minimizing the induced irradiation damage. The employed beam size was ∼65 nm, allowing the microanalysis of small clusters of several magnetosomes. Five spectra were acquired and averaged for each sample.

HRTEM measurements were carried out using a FEI Titan Cubed G2 60-300 electron microscope at 300 kV equipped with a high-brightness X-FEG Schottky field emission electron gun, a monochromator, and CEOS GmbH spherical aberration (C_s) corrector on the image side. The structural parameters of the magnetosomes were obtained by Fourier transform analysis.

X-ray Absorption Near-Edge Structure (XANES). XANES measurements were performed on isolated magnetosomes to maximize the signal-to-noise ratio. For these measurements, magnetosomes were freeze-dried and thoroughly mixed with boron nitride, the resultant mixture was compacted into 5 mm diameter pellets.

Measurements were performed at room temperature and atmospheric conditions at the branch A of BM25-SpLine of the ESRF synchrotron facility (France).[30] Fe and Mn foils were measured to calibrate the energy at the beginning and end of the experiment. In these conditions, the edge position of the sample can be determined with an accuracy of ΔE = 0.3 eV. Data for undoped magnetosomes (pure Fe_3O_4) and various Mn references were acquired in transmission mode (Fe and/or Mn K-edges). Mn(100) magnetosome spectra were acquired in transmission mode at the Fe K-edge and in fluorescence yield mode at the Mn K-edge. A number of three to five spectra were acquired and averaged for each sample to improve the signal-to-noise ratio. All data were treated using Athena software from the Iffefit package.[31]

X-ray Magnetic Circular Dichroism (XMCD). Room temperature XMCD experiments were performed using the ALICE station[32,33] at the PM3 beamline of BESSY II in Berlin, Germany. Data acquisition was achieved in transmission mode. A drop of 5 μL of purified magnetosomes in an aqueous solution was deposited onto 300 mesh carbon-coated Cu grids. The concentration of the magnetosome solution was optimized for the proper detection of Fe and Mn ions at
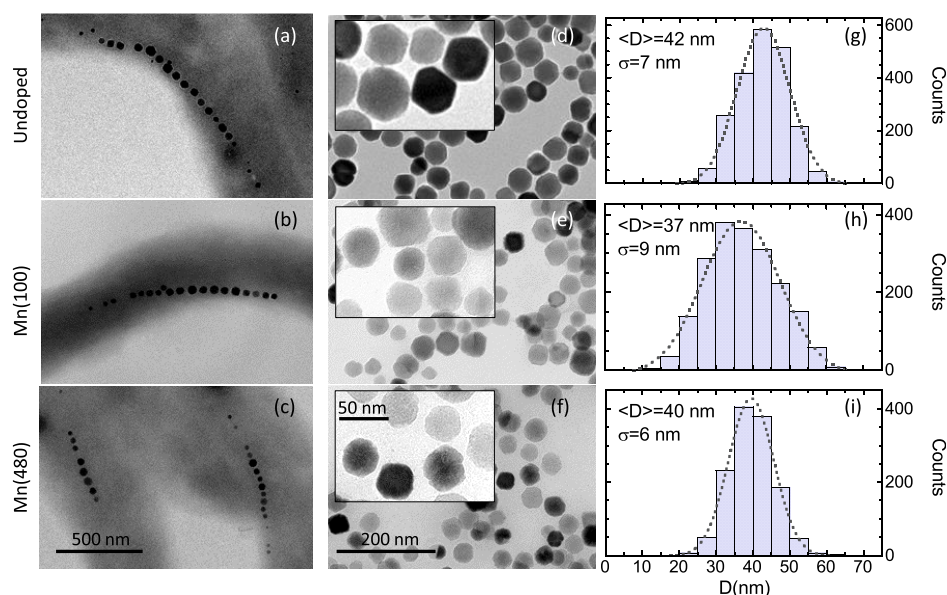
Figure 1. Representative TEM images of (a–c) *M. gryphiswaldense* and (d–f) isolated magnetosomes. Insets correspond to zoom-in images so as to highlight the observed morphological changes. (g–i) Size distribution for the undoped, Mn(100), and Mn(480) magnetosomes.
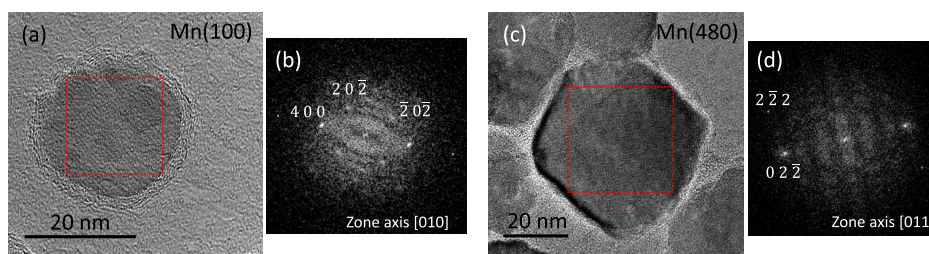

Figure 2. (a, c) HRTEM images of Mn(100) and Mn(480) magnetosomes and (b, d) Fourier transform images of isolated magnetosomes (red dotted squares).

their respective $L_{3,2}$-edges: 0.2 and 0.5 mg/mL Fe_3O_4 were used for the study of the undoped and Mn-doped magnetosomes at the Fe $L_{3,2}$-edges, respectively, while a 10 mg/mL Fe_3O_4-concentrated solution was used for the data acquisition at the Mn $L_{3,2}$-edges. X-ray radiation (circularly polarized, left helicity) impinged the sample surface at normal incidence. X-ray absorption spectra (I) were obtained across the Fe and Mn $L_{3,2}$-edges with a step size of 0.2 eV with an applied magnetic field parallel to the X-ray beam of +0.35 T (I^+) and −0.35 T (I^-). Three spectra were acquired and averaged to improve the signal-to-noise ratio. XMCD was defined as (I^+−I^-).

Theoretical spectra at the Mn $L_{3,2}$-edge were simulated considering tetrahedral and octahedral environments for Mn^{2+} and octahedral occupancy for Mn^{3+} with the spin orbit coupling acting on the 3d shell, the Slater integrals were scaled to κ = 80%. The crystal-field parameter $10Dq$ was fixed to 1.56 eV for octahedral sites and −0.6 eV for tetrahedral ones.[34] The calculated spectra were convoluted by a Lorentzian profile with a half-width half-maximum (HWHM) of Γ_{L_3}= 0.12 eV and Γ_{L_2}= 0.24 eV, to account for the intrinsic core-hole lifetime broadening, and a Gaussian function, σ = 0.15 eV HWHM, to account for the instrumental broadening. Spectra were simulated using the CTM4XAS program.[35]

Magnetic Measurements. The magnetic characterization was carried out on the freeze-dried cells. For that, the fixed and washed cells were highly concentrated and rapidly frozen by immersing them into liquid nitrogen. The frozen sample was immediately placed into a Telstar LyoQuest-85 plus freeze-dryer set at −85° C. The pressure and temperature control ensure the drying of the sample by sublimation, preserving the physical form of cells. The resulting powder sample was encapsulated in a gelatin capsule, giving rise to a structurally and magnetically isotropic sample where magnetosome chains are randomly oriented.[36] Magnetic measurements were carried out in a superconducting quantum interference device magnetometer (Quantum Design MPMS-3). Isothermal magnetization loops were measured between μ_0H = +1 and −1 T from T = 5–300 K after a cooling process with either no applied magnetic field [zero-field-cooling (ZFC)-$M(H)$] or under an applied magnetic field of 1 T [field-cooling FC-$M(H)$].

RESULTS AND DISCUSSION

Structural and Morphological Characterization. Figure 1a–f shows representative TEM images of *M. gryphiswaldense* and isolated magnetosomes for undoped, Mn(100), and Mn(480) samples. There are no significant differences in the cell morphology and chain arrangement between samples. The three cultures exhibit magnetosomes arranged in a single chain with a variable number of magnetosomes per cell between 10 and 30 (see the Supporting Information, Figure S1).

Figure 1g–i shows the particle size distributions determined from TEM images of the isolated magnetosomes, analyzing at least 1500 particles per sample to get reasonable statistics. The
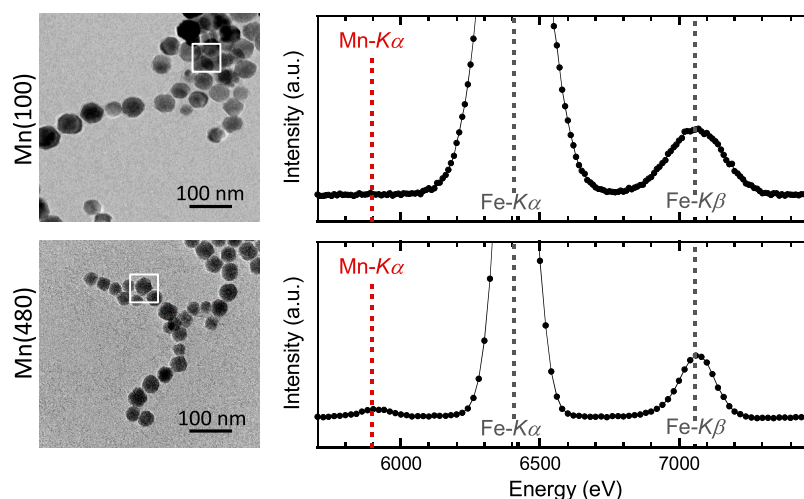
Figure 3. EDX spectra carried out on small clusters of Mn(100) and Mn(480) magnetosomes. The left panel presents TEM micrographs of magnetosome clusters in the region of interest. White squares delimit one out of the five EDX analyzed regions (beam size 65 nm). The right panel displays the average EDX spectra of the five single regions. Vertical dashed lines indicate the position of Mn Kα, Fe Kα, and Fe Kβ emission lines, respectively.
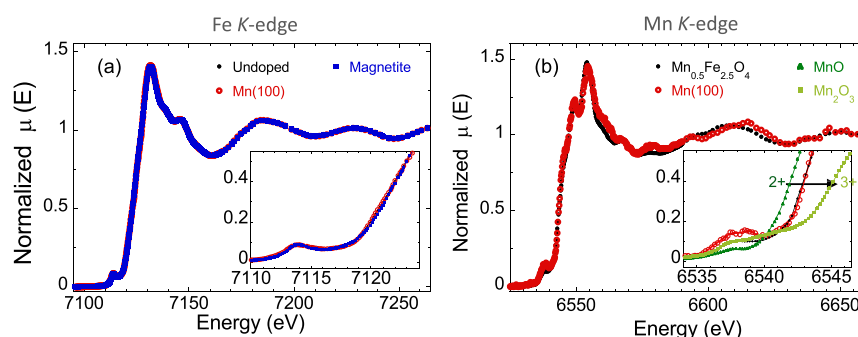

Figure 4. (a) Normalized Fe K-edge XANES spectra of undoped, Mn(100) magnetosomes, and bulk magnetite. The inset displays the pre-edge region in a more detailed depiction. (b) Normalized Mn K-edge XANES spectra of Mn(100) magnetosomes and $Mn_{0.5}Fe_{2.5}O_4$. The inset is a zoom-in of the Mn pre-edge region compared to commercial oxides: MnO (Mn^{2+}) and Mn_2O_3 (Mn^{3+}). The Fe and Mn K-edge pre-edge regions of all samples have been fitted (continuous lines) considering a set of Gaussian profile peaks (see the Supporting Information).

resulting histograms were fitted by a Gaussian function.[37,38] The undoped sample presents uniformly sized magnetosomes, as reflected in its corresponding histogram, where the size distribution is centered at $\langle D \rangle$ = 42 nm with a standard deviation σ = 7 nm. Mn(100) and Mn(480) magnetosomes present size distributions slightly shifted to lower values compared to the undoped magnetosomes. The size distribution of the Mn(100) peaks is centered at $\langle D \rangle$ = 37 nm (σ = 9 nm), while the distribution of the Mn(480) magnetosomes is centered at $\langle D \rangle$ = 40 nm (σ = 6 nm).

While previous reports on Mn doping of magnetosomes do not show any significant differences in the morphology or size,[16,20,21,26] TEM images presented in Figure 1 suggest certain morphological variations between samples. In particular, Mn-doped magnetosomes present more irregular edges as compared to the sharply faceted undoped particles.

Aiming to analyze the microstructural properties of the Mn-doped magnetosomes, high-resolution TEM (HRTEM) imaging was performed. Figure 2 shows a single particle of Mn(100) and Mn(480) together with the Fourier transform image of the marked region. Both samples manifest a set of well-defined lattice fringes. From the indexing of the diffraction spots observed in the Fourier transform image, we determined the crystalline structure of both nanoparticles. Mn(100) and

Mn(480) magnetosomes evidence a magnetite structure oriented in the [010] and the [011] zone axis, respectively. It indicates that the cubic spinel structure of the magnetite is not disturbed upon doping of Mn ions.

The chemical composition of isolated Mn magnetosomes was evaluated by means of energy-dispersive X-ray spectroscopy (EDX) in TEM mode. Figure 3 displays TEM micrographs of the extracted magnetosomes and the EDX spectra obtained by averaging five individual regions of the doped samples. Both samples show two main peaks attributed to the dominant presence of iron in the magnetosomes. The one at lower energies (~6400 eV) corresponds to the Fe Kα emission line and the one at higher energies (~7058 eV) to the Fe Kβ. The position of the Mn Kα emission line (~5899 eV) has been marked with a red dashed line in the experimental spectra. No evidence of Mn has been found in the Mn(100) sample indicating that the presence of such an element is below the resolution limit of the technique ($\approx$1 atomic %). An average value of 2.3 atomic % Mn was detected in the Mn(480) sample.

The coordination environment of the Fe and Mn ions in the magnetite structure has been investigated by means of X-ray absorption near-edge structure (XANES) and X-ray magnetic circular dichroism (XMCD) spectroscopies. XANES and
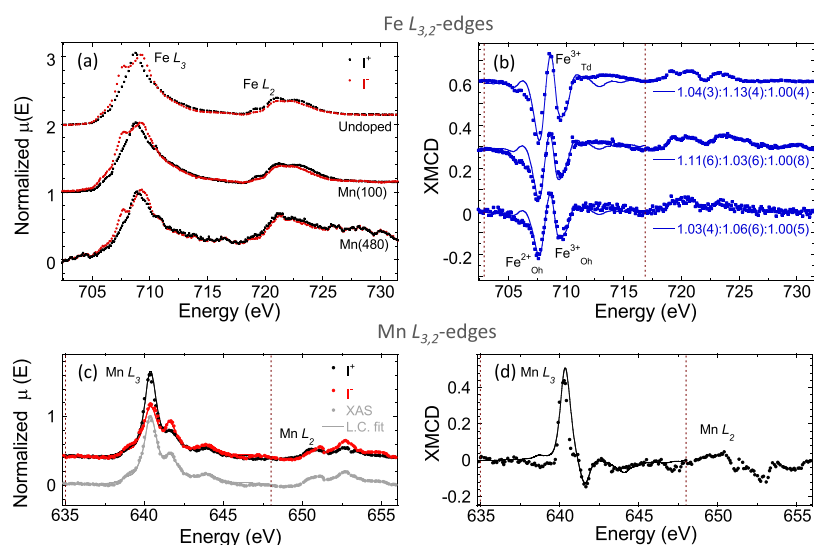
Figure 5. Transmission X-ray absorption spectra (XAS) acquired at $\pm$ 0.35 T ($I^\pm$) at the (a) Fe $L_{3,2}$-edges of undoped, Mn(100), and Mn(480) magnetosomes and (c) Mn $L_{3,2}$-edges of Mn(480) magnetosomes. Spectra have been normalized by the peak intensity at the L_3-edge of the nonmagnetic contribution of the XAS ($I^+ + I^-$)/2. The magnetic contributions (XMCD) given by ($I^+ - I^-$), are presented in (b, d). The continuous line presents the best theoretical simulation of the Fe L_3-edge XMCD spectra and Mn L_3-edge XAS and XMCD spectra in the energy window delimited by the vertical dotted lines (see the Supporting Information).

XMCD are very powerful techniques that provide accurate information on the oxidation state and site occupancy of the Mn cations in the spinel structure of the magnetite—where the Fe ions occupy three different sites: 8 Fe^{2+} in octahedral sites (O_h), 8 Fe^{3+} in tetrahedral (T_d) sites, and 8 Fe^{3+} in octahedral (O_h) ones.

Figure 4a shows the Fe K-edge XANES spectra of undoped and Mn(100) magnetosomes together with bulk magnetite. As previously reported by our group, undoped magnetosomes accurately reproduce the spectrum of magnetite,[18,39,40] and so do Mn-doped magnetosomes. This resemblance is also highlighted in the inset in Figure 4a, which exhibits an identical edge position and pre-edge feature of the three samples. This fact suggests an unperturbed coordination environment around the Fe-absorbing atoms in Mn(100) magnetosomes, agreeing with the imperceptible presence of Mn detected by EDX in this sample.

However, the presence of Mn in the magnetite structure is confirmed by the spectrum obtained at the Mn absorption edge, which exhibits a good signal-to-noise ratio. Figure 4b shows the Mn K-edge XANES spectrum of the Mn(100) magnetosomes together with the one of $Mn_{0.5}Fe_{2.5}O_4$ provided by Dr. Mazarío, which presents a cation distribution similar to Mn-ferrite.[41] At a first glance, we observe the similarity between both spectra indicating that Mn is introduced into the spinel structure of the magnetite.

By looking at the edge position and the pre-edge region we can infer the oxidation state and the symmetry of the Mn absorber atom. The inset in Figure 4b highlights the low-energy region of the Mn K-edge XANES spectrum of the Mn(100) magnetosomes together with that corresponding to MnO (Mn^{2+}) and Mn_2O_3 (Mn^{3+}) reference samples. The edge of the Mn(100) magnetosomes (6543.3 eV) appears between the edge position of MnO (6542.4 eV) and Mn_2O_3 (6546.0 eV). For similar compounds in which the absorbing element presents the same symmetry, there exists a linear relationship between the redox state and edge position.[42] In the present case, as will be shown later, the different Mn ions in the sample

could appear in different symmetries increasing the error associated with the quantification of the redox analysis of the edge.[43−46] A rough estimation taking into account that there is a total edge displacement of 3.6 eV from Mn^{2+} to Mn^{3+} spectra in octahedral compounds and a 0.9 eV shift occurring between the Mn(100) magnetosomes and MnO (Mn^{2+}) edges indicates that there are a majority of Mn^{2+} (75%) cations coexisting with Mn^{3+} cations (25%).

On the other hand, the intensity and position of the pre-edge region are also related to the redox state and symmetry of the absorber atom. The Mn K-edge XANES spectrum of the Mn(100) magnetosomes exhibits the pre-edge peak located around 5 eV before the edge position of the Mn K-edge, see Figure 4b. The high intensity of the pre-edge feature provides evidence for noncentrosymmetric tetrahedral sites.[42,43,47,48] Moreover, the multiple-peak pre-edge feature suggests a coexistence with centrosymmetric octahedral sites.[43] The centroid position of the Mn(100) magnetosomes, obtained from the fit to a set of Gaussian functions (see the Supporting Information), is located between the centroid position of MnO (Mn^{2+}) and Mn_2O_3 (Mn^{3+}), indicating a mixed valence state. However, the coexistence of the two oxidation states and symmetries proves cumbersome to obtain further quantitative information from the pre-edge region in the Mn(100) sample. We will use XMCD data to better clarify this point.

The site occupancy and oxidation state of Mn in the Mn-doped magnetosomes have been analyzed by means of XMCD at the Fe and Mn $L_{3,2}$-edges. The Fe $L_{3,2}$-edges ($I^\pm$) and the XMCD ($I^+ - I^-$) spectra of the undoped, Mn(100), and Mn(480) magnetosomes are depicted in Figure 5a,b. XMCD spectra show three main peaks characteristic of magnetite.[49,50] Those peaks are attributed to the different occupations of the Fe cations: the two negative peaks are mainly due to the octahedral occupation of Fe^{2+} and Fe^{3+} ions, while the positive peak between them is due to the Fe^{3+} ions placed in tetrahedral sites. The opposite sign of the peaks indicates the antiferromagnetic coupling between octahedral and tetrahedral sites in magnetite. From the experimental XMCD spectra we
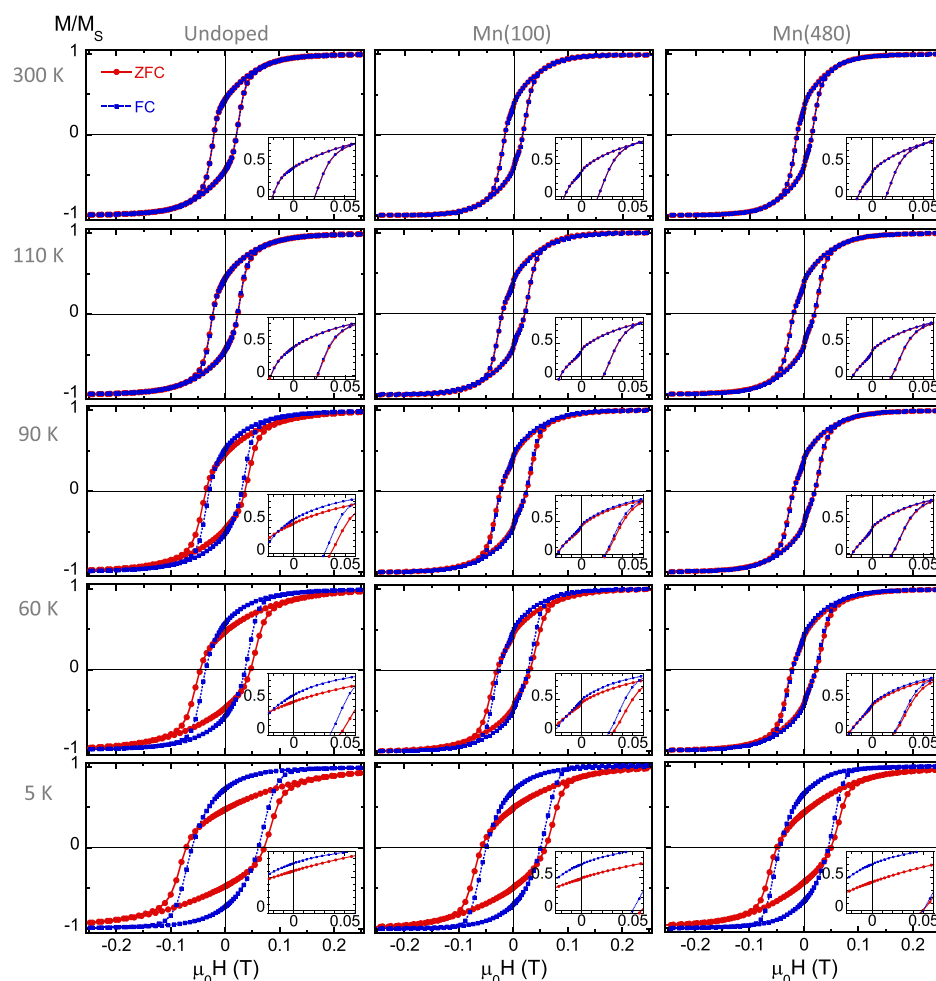
Figure 6. Comparison of experimental zero-field cooling (ZFC-$M(H)$) and field cooling (FC-$M(H)$) hysteresis loops of undoped, Mn(100), and Mn(480) magnetosomes at selected temperatures. The zoom-ins present more detailed depictions of the remanence region of the ZFC/FC-$M(H)$ loops where the kink is observed.

have determined the ratio $Fe_{Oh}^{2+}/Fe_{Td}^{3+}/Fe_{Oh}^{3+}$ by the linear combination fit of the theoretical spectra of the individual Fe components. The best linear combination fits of the Fe L_3-edge obtained between 703 and 717 eV have been superimposed, as shown in Figure 5b. The computed ratios obtained were 1.04(3):1.13(4):1.00(5) for undoped, 1.11(6):1.03(6):1.00(8) for Mn(100), and 1.03(4):1.06(6):1.00(5) for Mn(480) magnetosomes. The three calculated ratios are close to the expected ratio for stoichiometric magnetite (1:1:1).[18] As previously inferred from the Fe K-edge XANES spectrum of Mn(100) magnetosomes, the incorporation of Mn cations barely alters the coordination environment of the Fe absorbing atoms.

Figure 5c,d displays Mn L-edge XAS ($I^\pm$) and XMCD spectra of the Mn(480) magnetosomes, respectively. The Mn L-edge XAS and XMCD spectra corresponding to the Mn(100) sample can be found in the Supporting Information. We focused the analysis on the Mn(480) sample owing to the higher concentration of Mn in the sample and the better resolution of the Mn $L_{3,2}$-edges XAS and XMCD spectra. While the Mn(480) sample exhibits well-defined XAS and XMCD spectra, Mn(100) magnetosomes present less intense and noisier Mn L-edge peaks (see Figure S5 in the Supporting Information). Indeed, from the comparison of the intensity of the Mn L_3-edge XAS spectra of both samples, one can calculate

the relative Mn concentration between them. From there we determined that the Mn concentration in the Mn(480) magnetosomes is ≈ 2.13 higher than in the Mn(100) sample (see Table S3). This means that, since the Mn atomic percentage of Mn(480) magnetosomes determined by EDX was 2.3 atomic %, Mn(100) rounds 1 atomic % Mn.

To quantify the site occupancies, the experimental Mn L-edge XAS and the XMCD spectra of the Mn(480) sample were modeled using ligand field multiplet calculations of the individual Mn sites. Theoretical XAS spectra have been calculated for Mn^{3+} and Mn^{2+} cations in both tetrahedral and octahedral coordinations (see the Supporting Information). The experimental nonmagnetic contribution of XAS ((I^+ + I^-)/2) was fitted to a linear combination of the three calculated spectra between 635 and 648 eV. The best linear combination fit has been superimposed, as shown in Figure 5c,d and corresponds to 83.8(4)% Mn_{Td}^{2+}, 4.0(4)% Mn_{Oh}^{2+}, and 12.2(3)% Mn_{Oh}^{3+}.

The results obtained for the Mn(480) magnetosomes are in good agreement with those observed by XANES for the Mn(100) sample. Mn-doped magnetosomes present a dominant presence of Mn^{2+} cations occupying tetrahedral sites in coexistence with a minority of Mn cations, mostly Mn^{3+}, in the octahedral coordination. The obtained percentages reproduce the inversion degree reported in the
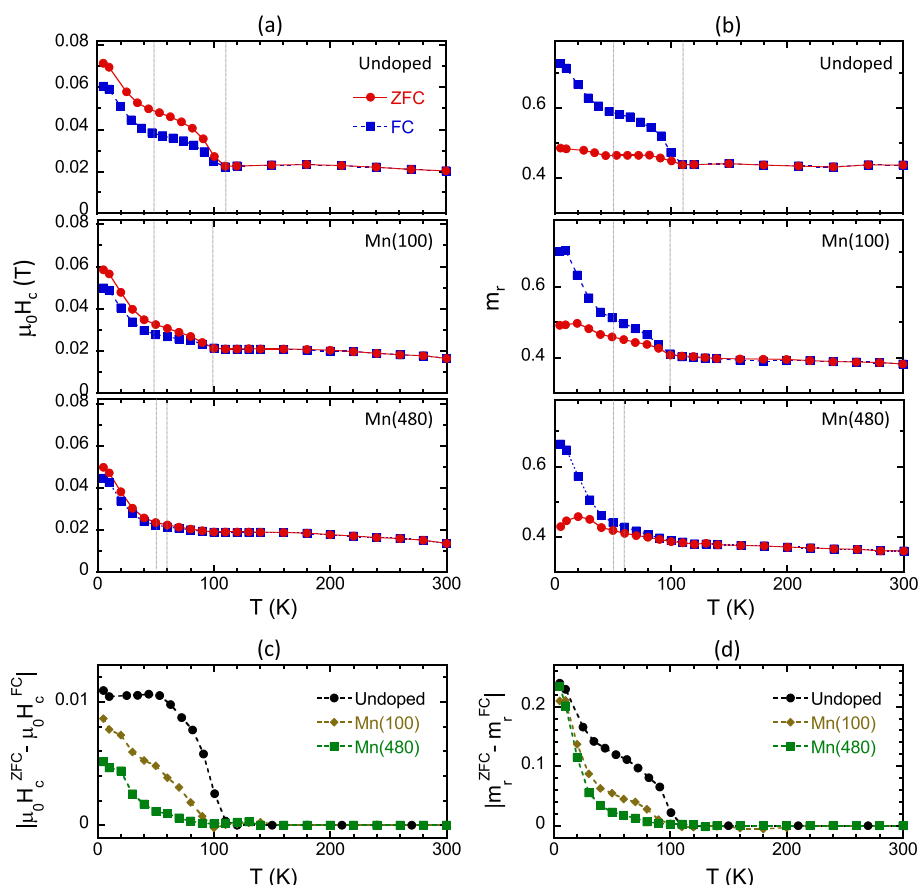
Figure 7. (a) Coercive field ($\mu_0 H_c$) and (b) reduced remanence magnetization (m_r) evolution as a function of the temperature for the undoped, Mn(100), and Mn(480) magnetosomes. ZFC and FC-$M(H)$ are compared. Temperature evolution of the difference (in absolute value) between ZFC and FC-$M(H)$ in the (c) $\mu_0 H_c$ and (d) m_r. Vertical dashed lines highlight the values at which the irreversibility between the ZFC and FC-$M(H)$ occurs: 107 K (undoped), 100 K (Mn(100)), and 60 K (Mn(480)), and the low temperature transition at 50 K.

bibliography for bulk Mn-ferrite[51−53] and ascribe the presence of Mn^{3+} cations to the inversion degree in Mn ferrites.[24,41,52]

Magnetic Measurements. To determine the role of Mn on the magnetic anisotropy of the doped magnetosomes, hereafter we present a complete magnetic characterization of undoped and Mn-doped magnetosomes as a function of temperature. All of the measurements have been carried out on the whole bacteria and hence on magnetosomes arranged in chains, where only intrachain interactions are expected.

Isothermal magnetization loops were measured after a cooling process with either no applied magnetic field (zero-field-cooling (ZFC)-$M(H)$) or under an applied magnetic field of 1 T (field-cooling (FC)-$M(H)$). ZFC/FC hysteresis loops of the three samples at selected temperatures are shown in Figure 6. In the case of the undoped sample, the ZFC and FC-$M(H)$ curves perfectly overlap down to T_V=107 K. At this temperature the well-known Verwey transition, involving a cubic-to-monoclinic crystallographic phase transition characteristic of magnetite, takes place.[40,54,55] Below the Verwey temperature there is an important dependence on the thermal history; the FC-$M(H)$ shows a decrease of the coercivity combined with a noticeable increase of the remanence with respect to the ZFC-$M(H)$. In contrast, the ZFC/FC-$M(H)$ of Mn(100) and Mn(480) magnetosomes overlap down to 100 and 60 K, respectively. Below these temperatures, differences between ZFC and FC-$M(H)$ emerge. Furthermore, clear changes in the shape of the loops are observed between the

samples. Contrary to the undoped magnetosomes, the ZFC/FC-$M(H)$ curves of Mn(100) and Mn(480) samples present a kink in the remanence region down to 100 and 60 K, respectively. Below these temperatures, the kink disappears. The presence of a kink is commonly related to the existence of two magnetic phases[56] but, and as will be shown later, the disappearance of the kink at low temperatures suggests a different origin. Finally, in comparison with the undoped magnetosomes, the ZFC/FC-$M(H)$ curves of Mn(100) and Mn(480) samples exhibit a reduction of the coercivity in the whole range of temperatures ($\approx$25 and $\approx$40%, respectively), in agreement with previous reports in the bibliography.[16,20,21]

The thermal evolution of the coercive field ($\mu_0 H_c^{ZFC/FC}$) and the reduced remanence magnetization ($m_r^{ZFC/FC} = (M_r/M_s)^{ZFC/FC}$) of the three samples can be easily tracked in Figure 7. For the undoped sample, both ZFC and FC-$M(H)$ present a nearly constant coercivity from 300 K down to T_V ($\mu_0 H_c^{ZFC/FC} \approx 22$ mT). Below the Verwey transition, the sample presents a marked irreversibility between $\mu_0 H_c^{ZFC}$ and $\mu_0 H_c^{FC}$. $\mu_0 H_c^{ZFC}$ increases up to 48 mT at 50 K, when a second transition attributed to the ordering of electron spins in magnetite at low temperature occurs.[57−59] Below that temperature, the coercive field steeply increases reaching values of 72 mT at 5 K. The FC-$M(H)$ exhibits similar but less intense features. Below the Verwey transition, $\mu_0 H^{FC}$ increases up to 39 mT at 50 K and rises up to 60 mT at 5 K. On the other hand, m_r^{ZFC} remains fairly constant between 0.44 and

0.49 throughout the whole temperature range. These values around 0.5 indicate that the undoped magnetosomes behave like randomly oriented uniaxial magnetic single domains in the framework of the Stoner−Wohlfarth model.[60] In contrast, when the field is applied in the cooling process, m_r^{FC} increases abruptly below the Verwey transition up to 0.6 at 50 K and up to 0.72 at 5 K.

The magnetic response of the Mn(100) and Mn(480) magnetosomes changes notably. The coercive fields of the ZFC/FC-$M(H)$ remain roughly constant down to 100 K, for the Mn(100) magnetosomes ($\mu_0 H_c^{ZFC/FC} \approx 20$ mT), and 60 K, in the case of the Mn(480) sample ($\mu_0 H_c^{ZFC/FC} \approx 15$ mT). Below these temperatures, the splitting of the ZFC and FC-$M(H)$ occurs. In the case of the $\mu_0 H_c^{ZFC}$, a smooth increase down to 50 K takes place. Beneath the low-temperature transition, $\mu_0 H_c^{ZFC}$ steeply rises up to 58 and 50 mT, respectively. Similarly, $\mu_0 H_c^{FC}$ rises softly at 50 K followed by the increase up to 50 mT (Mn(100)) and 44 mT (Mn(480)) at 5 K. On the other hand, the reduced remanence magnetizations of the ZFC/FC-$M(H)$ remain fairly constant down to 100 K ($m_r^{ZFC/FC} \approx 0.39$) and 60 K ($m_r^{ZFC/FC} \approx 0.36$), respectively. Below these temperatures, m_r^{ZFC} increases gradually equating the values obtained for the undoped magnetosomes at low temperature. In the case of the FC-$M(H)$, m_r^{FC} increases moderately down to 50 K and then rises up to 0.71 at 5 K, for the Mn(100) sample, and 0.66, in the case of Mn(480) magnetosomes.

The relative change of the coercive field and remanence magnetization between the ZFC and FC-$M(H)$ measurements as a function of temperature for the three samples can be tracked in Figures 7c,d. Here, it is clear that the divergence between the ZFC and FC-$M(H)$ values decreases with increasing Mn doping. The irreversibility between the ZFC and FC-$M(H)$ seems to root its origin in the Verwey transition, as will be discussed in the following section. Hence, it suggests that the cubic-to-monoclinic crystallographic phase transition still occurs in the presence of Mn cations but it is shifted from 107 K (undoped magnetosomes) to 100 K for the Mn(100) sample, and down to 60 K, for the Mn(480) magnetosomes. Similar results are inferred from the conventional ZFC and FC $M(T)$ curves presented in Figure S7 in the Supporting Information and previously reported by Prozorov and co-workers.[21] It is worth noting that the temperature values at which the split occurs coincide with the ones in which the kink of the $M(H)$ curves becomes negligible.

Magnetic Model. Aiming to understand the role of Mn in the magnetic properties of the doped magnetosomes, with special focus on their magnetic anisotropy, we have carried out numerical simulations of the magnetization dynamics of the magnetosomes. These have been computed at different temperatures considering a Stoner−Wohlfarth model with some pertinent modifications, as described previously by our group.[18,61,62] To achieve clear cut conclusions, we have selected the Mn(480) sample, which has evidenced more distinct magnetic differences compared to the undoped magnetosomes. Precisely, we just remind here that Mn(100) magnetosomes exhibit an intermediate behavior. All of the simulations presented here were performed considering a single magnetic phase.

In brief, magnetosome chains were considered as a collection of independent single domain nanoparticles large enough to be thermally stable and so to have the magnetization firmly anchored at the minimum energy states. Therefore, the

physical problem can be implemented using a single particle approach described by Stoner−Wohlfarth. Interparticle dipolar interactions occurring between the nearest magnetosome neighbors in the chain are assumed to impose an additional anisotropy contribution, equal for all.[63−65] Note that the chain−chain interactions in the freeze-dried cells are negligible due to the large distance separating two chains of magnetosomes.[36,66] The equilibrium orientation of each magnetic dipole is therefore calculated by minimizing the single dipole energy density, E, which is computed as the sum of three contributions:[18,61]

(i) The first term of the single dipole energy density is the cubic magnetocrystalline energy (E_c)

$$E_c(\theta, \varphi) = K_c \frac{[\sin^4(\theta)\sin^2(2\varphi) + \sin^2(2\theta)]}{4} \quad (1)$$

K_c being the cubic anisotropy constant and θ and φ the polar and azimuthal angles in spherical coordinates, respectively, of the magnetic moment ($\hat{u}_m$) considering the $\langle 100 \rangle$ crystallographic directions as the reference system (see the Supporting Information, Figure S8).

(ii) An effective uniaxial anisotropy contribution along the $\hat{u}_{uni}$ axis arising from the competition between the magnetosome shape anisotropy and the interparticle dipolar interactions between the closest magnetosome neighbors in the chain

$$E_{uni}(\theta, \varphi) = K_{uni}[1 - (\hat{u}_{uni}\cdot\hat{u}_m)^2] \quad (2)$$

where K_{uni} is the uniaxial anisotropy constant. On the basis of the previously reported chain configuration of undoped magnetosomes in *M. gryphiswaldense*, and for the sake of simplicity, the direction of the uniaxial axis $\hat{u}_{uni}$ has been fixed at 25° out of the chain axis (which corresponds to the [111] crystallographic easy axis of magnetite), toward the $\langle 110 \rangle$ direction.[61,67]

(iii) The Zeeman energy (E_{Zeeman}) in an external magnetic field $\mu_0 \vec{H}$ given by

$$E_{Zeeman}(\theta, \varphi) = -\mu_0 M H(\hat{u}_H\cdot\hat{u}_m) \quad (3)$$

where $\hat{u}_H$ represents the external magnetic field unit vector.

Thus, the single dipole energy density E is described as

$$E(\theta, \varphi) = E_c(\theta, \varphi) + E_{uni}(\theta, \varphi) + E_{Zeeman}(\theta, \varphi) \quad (4)$$

Under these considerations, the ZFC/FC-$M(H)$ loops at different temperatures have been simulated assuming a dynamical approach described elsewhere.[61,68,69] K_c and K_{uni} have been adjusted to achieve the best match between the experiment and theory. K_c and K_{uni} values found in simulations are presented in Figure 9 and will be discussed hereafter. As shown in Figure 8a−d, the simulated curves accurately reproduce the experimental hysteresis loops of the Mn(480) magnetosomes including the observed kink present in the remanence region down to 60 K. As shown in the Supporting Information, Figure S9, the presence or absence of this kink depends on the ratio r between the absolute value of the cubic anisotropy constant and the uniaxial anisotropy constant, $r = |K_c|/|K_{uni}|$, so that for $r > 1$ a clear kink is observed, while for $r \leq 1$ the kink is not distinguished anymore. Contrary to the undoped magnetosomes, where $r \leq 1$ from 300 K to T_V,[18] the Mn(480) magnetosomes show a ratio $r > 1$ down to the Verwey transition, giving rise to the observed kink (see the
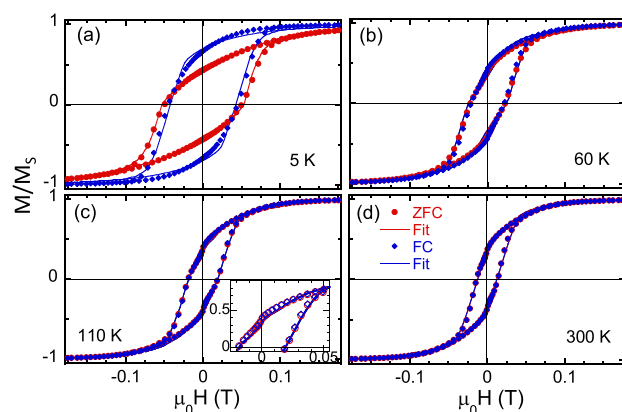
Figure 8. ZFC/FC-$M(H)$ loops of the Mn(480) magnetosomes measured at (a) 5 K, (b) 60 K, (c) 110 K, and (d) 300 K. Continuous lines correspond to the simulated loops considering the anisotropy constants presented in Figure 9. The inset highlights the reproducibility of the kink at 110 K.

Supporting lnformation Figure S10). As described hereafter, below the Verwey transition the anisotropy becomes essentially uniaxial, being the reason why the kink disappears below T_V.

The thermal evolution obtained for K_c and K_{uni} for the Mn(480) magnetosomes, as well as for the undoped sample (extracted from Marcano et al.[18]) is shown in Figure 9.

From the simulation, we find that K_c is negative from 300 K down to 60 K. The absolute value of K_c ($|K_c|$) increases from 10.80 kJ/m^3 at 300 K to 16.00 kJ/m^3 at 110 K. Then, $|K_c|$ slightly decreases down to 14 kJ/m^3 at 60 K. Below this temperature the experimental $M(H)$ loops present an essentially uniaxial behavior and the role of the cubic magnetocrystalline anisotropy becomes negligible in the simulation. In comparison with the undoped magnetosomes, the incorporation of Mn$^{2+,3+}$ into the spinel structure of magnetite introduces an additional negative contribution to the cubic magnetocrystalline energy. The whole trend as well as the obtained anisotropy values of K_c agree with the results reported in the late fifties in single crystals of Mn-substituted magnetite considering a concentration of Mn around 3 atomic %.[70,71] On the other hand, K_{uni} remains constant (slightly varying between 8 and 10 kJ/m^3) from the room temperature down to 60 K. As mentioned above, K_{uni} stems from the competition between the magnetosome shape anisotropy and the strength of the dipolar magnetic interactions, both depending only slightly on the temperature in this range. A similar tendency was observed for undoped magnetosomes

from 300 K to T_V, reporting values around 11−13 kJ/m^3 [18,61,72]. The reduction of the ≈25% observed in K_{uni} arises from the competition of the two anisotropy terms: the shape anisotropy and the dipolar interactions. No substantial differences were observed in the size and the arrangement of the magnetosomes within the bacteria that might affect the dipolar magnetic interactions although slight variations on the magnetic moment of the magnetosomes may occur as a consequence of Mn doping. On the other hand, TEM images show a modification of the shape of the magnetosomes with Mn doping. The presence of softly faceted magnetosomes could alter the shape anisotropy, and hence, the K_{uni}. Below 60 K, K_{uni} in the Mn(480) magnetosomes suddenly increases up to 27 kJ/m^3, also mimicking the trend of the undoped magnetosomes below T_V. When the cubic-to-monoclinic transition takes place, the magnetocrystalline anisotropy of the undoped sample changes from cubic to essentially uniaxial along the ⟨100⟩ crystallographic directions. Thus, the effective uniaxial anisotropy results from the competition of the magnetocrystalline anisotropy, shape anisotropy, and dipolar magnetic interactions with neighboring magnetosomes in the chain.

Finally, the differences observed between the FC and ZFC cases are attributed to the orientation distribution of the monoclinic axis below the Verwey transition. It is well known that cooling under an applied magnetic field triggers the unequivalency of the three ⟨100⟩ monoclinic axes, setting the easy magnetization axis along that ⟨100⟩ direction that is closer to the direction of the applied field.[70] However, aiming to reproduce the experimental hysteresis loops of the magnetosomes at low temperature, we further need to assume an intrinsic discrimination of the three ⟨100⟩ crystallographic directions. That is, in the absence of an applied field, the orthorhombic deformation would preferentially take place along the ⟨100⟩ direction closer to the easy magnetization axis of each magnetosome ($\hat{u}_{uni}$, which points 25° out of the chain axis toward the ⟨110⟩).[61,67] In contrast, when an external field is applied in the cooling process, the three ⟨100⟩ directions become equally probable. Thus, in the FC measurements, two-thirds of the orthorhombic deformation will take place along the ⟨100⟩ direction closer to $\hat{u}_{uni}$, and one-third will occur in the remaining ⟨100⟩ direction. The latter is approximately perpendicular to $\hat{u}_{uni}$, so strongly competes with it. As a consequence, this gives rise to a decrease of the effective uniaxial anisotropy in the FC case with respect to the ZFC, which explains the experimentally observed decrease in the coercive field in the FC situation (see Figure 8 and the Supporting Information, Figure S11).
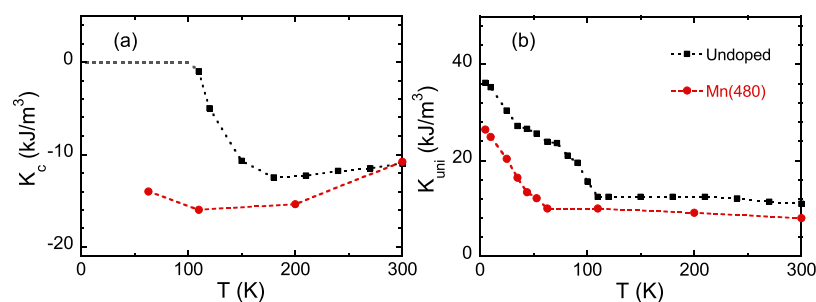

Figure 9. Best theoretical−experimental matching values for (a) cubic magnetocrystalline, K_c and (b) uniaxial anisotropy, K_{uni}, constants obtained for Mn(480) compared to undoped magnetosomes (extracted from Marcano et al.[18]).

CONCLUSIONS

In conclusion, we carried out a complete study on the Mn doping of magnetosomes within *M. gryphiswaldense* MSR-1. Using two different culture media differing in the Mn concentration we have demonstrated the possibility to obtain Mn doping grade magnetosomes. This opens up the possibility to tune the magnetic properties under ambient conditions for a range of advanced biomedical applications.

From the combination of structural techniques we have detected up to 2.3 atomic % Mn incorporated in the crystallographic structure of the magnetite, with a dominant presence of Mn^{2+} in the tetrahedral coordination coexisting with a minority of Mn ions, predominantly Mn^{3+}, in the octahedral coordination. The Mn doping of the magnetosomes results in a notable change of their magnetic properties, which has been addressed by a complete magnetic characterization based on the study of the ZFC/FC-$M(H)$ loops as a function of temperature. Prominent among these are a reduction of the coercive field concomitant with a shift of the Verwey transition to lower temperatures with increasing Mn doping. On the basis of the slightly modified Stoner−Wohlfarth model and considering the different anisotropy contributions, we have been able to accurately reproduce the magnetic behavior of Mn-doped magnetosomes. This has allowed us to shed light on the role of Mn incorporation in the magnetocrystalline anisotropy of the magnetosomes, which accurately reproduced the behavior classically observed in single crystals of Mn-substituted magnetites. Furthermore, we observed a decrease in the effective uniaxial anisotropy attributed to the modification of the shape of the doped magnetosomes, also suggested by TEM imaging.

ASSOCIATED CONTENT

Ⓢ Supporting Information

The Supporting Information is available free of charge at https://pubs.acs.org/doi/10.1021/acs.jpcc.0c07018.

Analysis of the influence of Mn in the number of magnetosomes per chain; Fe K-edge XANES spectra comparison of bulk magnetite and maghemite with undoped and Mn(100) magnetosomes; pre-edge fits at Fe and Mn K-edges; determination of the relative Mn concentration between Mn(100) and Mn(480) magnetosomes from Mn L-edge XAS spectroscopy; details of XMCD simulations; zero-field cooling/field cooling (ZFC-FC)-$M(H)$ curves; reference frame used in the magnetic simulations; role of the ratio $r = |K_c|/|K_{uni}|$; simulations of ZFC and FC-$M(H)$ loops of undoped magnetosomes at 5 K (PDF)

AUTHOR INFORMATION

Corresponding Author

Lourdes Marcano − *Helmholtz-Zentrum Berlin für Materialien und Energie, 12489 Berlin, Germany; Dpto. Electricidad y Electrónica, Universidad del País Vasco—UPV/EHU, 48940 Leioa, Spain;* ⓞ orcid.org/0000-0001-9397-6122; Email: lourdes.marcano@ehu.eus

Authors

Iñaki Orue − *SGIker, Universidad del País Vasco—UPV/EHU, 48940 Leioa, Spain*

Ana García-Prieto − *Departmento Física Aplicada I, Universidad del País Vasco—UPV/EHU, 48013 Bilbao, Spain; BCMaterials, Bld. Martina Casiano 3rd floor, 48940 Leioa, Spain*

Radu Abrudan − *Helmholtz-Zentrum Berlin für Materialien und Energie, 12489 Berlin, Germany*

Javier Alonso − *CITIMAC, Universidad de Cantabria, 39005 Santander, Spain;* ⓞ orcid.org/0000-0003-0045-5390

Luis Fernández Barquín − *CITIMAC, Universidad de Cantabria, 39005 Santander, Spain*

Sergio Valencia − *Helmholtz-Zentrum Berlin für Materialien und Energie, 12489 Berlin, Germany;* ⓞ orcid.org/0000-0002-3912-5797

Alicia Muela − *Departmento Inmunología, Microbiología y Parasitología, Universidad del País Vasco—UPV/EHU, 48940 Leioa, Spain; BCMaterials, Bld. Martina Casiano 3rd floor, 48940 Leioa, Spain*

M. Luisa Fdez-Gubieda − *Dpto. Electricidad y Electrónica, Universidad del País Vasco—UPV/EHU, 48940 Leioa, Spain; BCMaterials, Bld. Martina Casiano 3rd floor, 48940 Leioa, Spain;* ⓞ orcid.org/0000-0001-6076-7738

Complete contact information is available at:
https://pubs.acs.org/10.1021/acs.jpcc.0c07018

Notes

The authors declare no competing financial interest.

REFERENCES

(1) Bazylinski, D. A.; Frankel, R. B. Magnetosome formation in prokaryotes. *Nat. Rev. Microbiol.* **2004**, *2*, 217−230.

(2) Bazylinski, D. A.; Lefèvre, C. T.; Schüler, D. *The Prokaryotes*; Rosenberg, E.; DeLong, E. F.; Lory, S.; Stackebrandt, E.; Thompson, F., Eds.; Springer Berlin Heidelberg: Berlin, Heidelberg, 2013; pp 453−494.

(3) Bazylinski, D. A.; Lefèvre, C. T.; Lower, B. H. *Nanomicrobiology*; Barton, L. L.; Bazylinski, D. A.; Xu, H., Eds.; Springer: New York, 2014; Chapter 3, pp 39−74.

(4) Uebe, R.; Schüler, D. Magnetosome biogenesis in magnetotactic bacteria. *Nat. Rev. Microbiol.* **2016**, *14*, 621−637.

(5) Alphandéry, E. Applications of Magnetosomes Synthesized by Magnetotactic Bacteria in Medicine. *Front. Bioeng. Biotechnol.* **2014**, *2*, 5.

(6) Muela, A.; Muñoz, D.; Martín-Rodríguez, R.; Orue, I.; Garaio, E.; Abad Díaz de Cerio, A.; Alonso, J.; García, J. Á.; Fdez-Gubieda, M. L. Optimal Parameters for Hyperthermia Treatment Using Biomineralized Magnetite Nanoparticles: Theoretical and Experimental Approach. *J. Phys. Chem. C* **2016**, *120*, 24437−24448.

(7) Sun, J.; Tang, T.; Duan, J.; Xu, P.-x.; Wang, Z.; Zhang, Y.; Wu, L.; Li, Y. Biocompatibility of bacterial magnetosomes: Acute toxicity, immunotoxicity and cytotoxicity. *Nanotoxicology* **2010**, *4*, 271−283.

(8) Mannucci, S.; Ghin, L.; Conti, G.; Tambalo, S.; Lascialfari, A.; Orlando, T.; Benati, D.; Bernardi, P.; Betterle, N.; Bassi, R.; et al.

Magnetic Nanoparticles from *Magnetospirillum gryphiswaldense* Increase the Efficacy of Thermotherapy in a Model of Colon Carcinoma. *PLoS One* **2014**, *9*, No. e108959.

(9) Orlando, T.; Mannucci, S.; Fantechi, E.; Conti, G.; Tambalo, S.; Busato, A.; Innocenti, C.; Ghin, L.; Bassi, R.; Arosio, P.; et al. Characterization of magnetic nanoparticles from *Magnetospirillum gryphiswaldense* as potential theranostics tools: Characterization of Magnetic Nanoparticles from Magnetotactic Bacteria. *Contrast Media Mol. Imaging* **2016**, *11*, 139−145.

(10) Martel, S. Targeting active cancer cells with smart bullets. *Ther. Delivery* **2017**, *8*, 301−312.

(11) Felfoul, O.; Mohammadi, M.; Taherkhani, S.; de Lanauze, D.; Zhong Xu, Y.; Loghin, D.; Essa, S.; Jancik, S.; Houle, D.; Lafleur, M.; et al. Magneto-aerotactic bacteria deliver drug-containing nanoliposomes to tumour hypoxic regions. *Nat. Nanotechnol.* **2016**, *11*, 941−947.

(12) Mathuriya, A. S. Magnetotactic bacteria: nanodrivers of the future. *Crit. Rev. Biotechnol.* **2016**, *36*, 788−802.

(13) Gandia, D.; Gandarias, L.; Rodrigo, I.; Robles-García, J.; Das, R.; Garaio, E.; García, J. A.; Phan, M.; Srikanth, H.; Orue, I. Unlocking the Potential of Magnetotactic Bacteria as Magnetic Hyperthermia Agents. *Small* **2019**, *15*, 1902626.

(14) Larumbe, S.; Gomez-Polo, C.; Pérez-Landazábal, J. I.; García-Prieto, A.; Alonso, J.; Fdez-Gubieda, M. L.; Cordero, D.; Gómez, J. Ni Doped Fe₃O₄ Magnetic Nanoparticles. *J. Nanosci. Nanotechnol.* **2012**, *12*, 2652−2660.

(15) Staniland, S.; Williams, W.; Telling, N.; Van Der Laan, G.; Harrison, A.; Ward, B. Controlled cobalt doping of magnetosomes in vivo. *Nat. Nanotechnol.* **2008**, *3*, 158−162.

(16) Tanaka, M.; Brown, R.; Hondow, N.; Arakaki, A.; Matsunaga, T.; Staniland, S. Highest levels of Cu, Mn and Co doped into nanomagnetic magnetosomes through optimized biomineralisation. *J. Mater. Chem.* **2012**, *22*, 11919−11921.

(17) Li, J.; Menguy, N.; Arrio, M.-A.; Sainctavit, P.; Juhin, A.; Wang, Y.; Chen, H.; Bunau, O.; Otero, E.; Ohresser, P.; et al. Controlled cobalt doping in the spinel structure of magnetosome magnetite: new evidences from element- and site-specific X-ray magnetic circular dichroism analyses. *J. R. Soc., Interface* **2016**, *13*, No. 20160355.

(18) Marcano, L.; Muñoz, D.; Martín-Rodríguez, R.; Orue, I.; Alonso, J.; García-Prieto, A.; Serrano, A.; Valencia, S.; Abrudan, R.; Fernández Barquín, L.; et al. Magnetic Study of Co-Doped Magnetosome Chains. *J. Phys. Chem. C* **2018**, *122*, 7541−7550.

(19) Alphandèry, E.; Carvallo, C.; Menguy, N.; Chebbi, I. Chains of Cobalt Doped Magnetosomes Extracted from AMB-1 Magnetotactic Bacteria for Application in Alternative Magnetic Field Cancer Therapy. *J. Phys. Chem. C* **2011**, *115*, 11920−11924.

(20) Pérez-Gonzalez, T.; Prozorov, T.; Yebra-Rodríguez, A.; Bazylinski, D.; Jimenez-López, C. Mn incorporation in magnetosomes: New possibilities for the nanotechnological applications of biomagnetite. *Macla* **2010**, *13*, 171.

(21) Prozorov, T.; Perez-Gonzalez, T.; Valverde-Tercedor, C.; Jimenez-Lopez, C.; Yebra-Rodriguez, A.; Körnig, A.; Faivre, D.; Mallapragada, S. K.; Howse, P. A.; Bazylinski, D. A.; et al. Manganese incorporation into the magnetosome magnetite: magnetic signature of doping. *Eur. J. Mineral.* **2014**, *26*, 457−471.

(22) Muñoz, D.; Marcano, L.; Martín-Rodríguez, R.; Simonelli, L.; Serrano, A.; García-Prieto, A.; Fdez-Gubieda, M. L.; Muela, A. Magnetosomes could be protective shields against metal stress in magnetotactic bacteria. *Sci. Rep.* **2020**, *10*, No. 11430.

(23) Goldman, A. *Modern Ferrite Technology*; Springer Science & Business Media, 2006.

(24) Vamvakidis, K.; Katsikini, M.; Vourlias, G.; Angelakeris, M.; Paloura, E. C.; Dendrinou-Samara, C. Composition and hydrophilicity control of Mn-doped ferrite (MnₓFe₃₋ₓO₄) nanoparticles induced by polyol differentiation. *Dalton Trans.* **2015**, *44*, 5396−5406.

(25) Lasheras, X.; Insausti, M.; de la Fuente, J. M.; Gil de Muro, I.; Castellanos-Rubio, I.; Marcano, L.; Fernández-Gubieda, M. L.; Serrano, A.; Martín-Rodríguez, R.; Garaio, E.; et al. Mn-Doping

level dependence on the magnetic response of MnₓFe₃₋ₓO₄ ferrite nanoparticles. *Dalton Trans.* **2019**, *48*, 11480−11491.

(26) Keim, C. N.; Lins, U.; Farina, M. Manganese in biogenic magnetite crystals from magnetotactic bacteria. *FEMS Microbiol. Lett.* **2009**, *292*, 250−253.

(27) Heyen, U.; Schüler, D. Growth and magnetosome formation by microaerophilic *Magnetospirillum* strains in an oxygen-controlled fermentor. *Appl. Microbiol. Biotechnol.* **2003**, *61*, 536−544.

(28) Grunberg, K.; Wawer, C.; Tebo, B. M.; Schuler, D. A Large Gene Cluster Encoding Several Magnetosome Proteins Is Conserved in Different Species of Magnetotactic Bacteria. *Appl. Environ. Microbiol.* **2001**, *67*, 4573−4582.

(29) Schneider, C. A.; Rasband, W. S.; Eliceiri, K. W. NIH Image to ImageJ: 25 years of image analysis. *Nat. Methods* **2012**, *9*, 671.

(30) Castro, G. R. Optical design of the general-purpose Spanish X-ray beamline for absorption and diffraction. *J. Synchrotron Radiat.* **1998**, *5*, 657−660.

(31) Ravel, B.; Newville, M. ATHENA, ARTEMIS, HEPHAESTUS: data analysis for X-ray absorption spectroscopy using IFEFFIT. *J. Synchrotron Radiat.* **2005**, *12*, 537−541.

(32) Grabis, J.; Nefedov, A.; Zabel, H. Diffractometer for soft x-ray resonant magnetic scattering. *Rev. Sci. Instrum.* **2003**, *74*, 4048−4051.

(33) Abrudan, R.; Brussing, F.; Salikhov, R.; Meermann, J.; Radu, I.; Ryll, H.; Radu, F.; Zabel, H. ALICE - An advanced reflectometer for static and dynamic experiments in magnetism at synchrotron radiation facilities. *Rev. Sci. Instrum.* **2015**, *86*, 063902.

(34) Å Tichauer, L.; Mirone, A.; Turchini, S.; Prosperi, T.; Zennaro, S.; Zema, N.; Lama, F.; Pontin, R.; ÅimÅ!a, Z.; Tailhades, P.; et al. X-ray absorption spectroscopy and magnetic circular dichroism of the Mn-ferrite nanocrystalline thin films. *J. Appl. Phys.* **2001**, *90*, 2511−2516.

(35) Stavitski, E.; de Groot, F. M. The CTM4XAS program for EELS and XAS spectral shape analysis of transition metal L edges. *Micron* **2010**, *41*, 687−694.

(36) Bender, P.; Marcano, L.; Orue, I.; Alba Venero, D.; Honecker, D.; Fernández Barquín, L.; Muela, A.; Fdez-Gubieda, M. L. Probing the stability and magnetic properties of magnetosome chains in freeze-dried magnetotactic bacteria. *Nanoscale Adv.* **2020**, *2*, 1115−1121.

(37) Arato, B. Crystal-size and shape distributions of magnetite from uncultured magnetotactic bacteria as a potential biomarker. *Am. Mineral.* **2005**, *90*, 1233−1240.

(38) Pósfai, M.; Cziner, K.; Máton, E.; Márton, P.; Buseck, P. R.; Frankel, R. R.; Bazylinski, D. A. Crystal-size distributions and possible biogenic origin of Fe sulfides. *Eur. J. Mineral.* **2001**, *13*, 691−703.

(39) Fdez-Gubieda, M. L.; Muela, A.; Alonso, J.; Garcia-Prieto, A.; Olivi, L.; Fernandez-Pacheco, R.; Barandiaran, J. M. Magnetite Biomineralization in *Magnetospirillum gryphiswaldense*: Time-Resolved Magnetic and Structural Studies. *ACS Nano* **2013**, *7*, 3297−3305.

(40) Marcano, L.; García-Prieto, A.; Muñoz, D.; Fernández Barquín, L.; Orue, I.; Alonso, J.; Muela, A.; Fdez-Gubieda, M. Influence of the bacterial growth phase on the magnetic properties of magnetosomes synthesized by *Magnetospirillum gryphiswaldense*. *Biochim. Biophys. Acta, Gen. Subj.* **2017**, *1861*, 1507−1514.

(41) Mazarío, E.; Mayoral, A.; Salas, E.; Menéndez, N.; Herrasti, P.; Sanchez-Marcos, J. Synthesis and characterization of manganese ferrite nanoparticles obtained by electrochemical/chemical method. *Mater. Des.* **2016**, *111*, 646−650.

(42) Fdez-Gubieda, M. L.; García-Prieto, A.; Alonso, J.; Meneghini, C. X-Ray Absorption Fine Structure Spectroscopy in Fe Oxides and Oxyhydroxides. In *Iron Oxides: From Nature to Applications*; Faivre, D., Ed.; Wiley-VCH, 2016; pp 397−422.

(43) Farges, F. *Ab initio* and experimental pre-edge investigations of the Mn K -edge XANES in oxide-type materials. *Phys. Rev. B* **2005**, *71*, No. 155109.

(44) Bargar, J.; Tebo, B.; Villinski, J. In situ characterization of Mn(II) oxidation by spores of the marine Bacillus sp. strain SG-1. *Geochim. Cosmochim. Acta* **2000**, *64*, 2775−2778.

(45) McKeown, D. A.; Post, J. E. Characterization of manganese oxide mineralogy in rock varnish and dendrites using X-ray absorption spectroscopy. *Am. Mineral.* **2001**, *86*, 701−713.

(46) McKeown, D. A.; Kot, W. K.; Gan, H.; Pegg, I. L. X-ray absorption studies of manganese valence and local environment in borosilicate waste glasses. *J. Non-Cryst. Solids* **2003**, *328*, 71−89.

(47) Wilke, M.; Farges, F.; Petit, P.-E.; E. Brown, G., Jr.; Martin, F. Oxidation state and coordination of Fe in minerals: An Fe K-XANES spectroscopy study. *Am. Mineral.* **2001**, *86*, 714−730.

(48) Westre, T. E.; Kennepohl, P.; DeWitt, J. G.; Hedman, B.; Hodgson, K. O.; Solomon, E. I. Multiplet Analysis of Fe K-Edge 1s → 3d Pre-Edge Features of Iron Complexes. *J. Am. Chem. Soc.* **1997**, *119*, 6297−6314.

(49) van der Laan, G.; Figueroa, A. I. X-ray magnetic circular dichroism—A versatile tool to study magnetism. *Coord. Chem. Rev.* **2014**, *277-278*, 95−129.

(50) Pattrick, R. A. D.; Van Der Laan, G.; Henderson, C. M. B.; Kuiper, P.; Dudzik, E.; Vaughan, D. J. Cation site occupancy in spinel ferrites studied by X-ray magnetic circular dichroism: developing a method for mineralogists. *Eur. J. Mineral.* **2002**, *14*, 1095−1102.

(51) O'Handley, R. *Modern Magnetic Materials: Principles and Applications*; Wiley, 1999.

(52) Carta, D.; Casula, M. F.; Mountjoy, G.; Corrias, A. Formation and cation distribution in supported manganese ferrite nanoparticles: an X-ray absorption study. *Phys. Chem. Chem. Phys.* **2008**, *10*, 3108−3117.

(53) Liang, X.; Zhong, Y.; Zhu, S.; He, H.; Yuan, P.; Zhu, J.; Jiang, Z. The valence and site occupancy of substituting metals in magnetite spinel structure $Fe_{3−x}M_xO_4$ (M = Cr, Mn, Co and Ni) and their influence on thermal stability: An XANES and TG-DSC investigation. *Solid State Sci.* **2013**, *15*, 115−122.

(54) Walz, F. The Verwey transition - a topical review. *J. Phys. Condens. Matter.* **2002**, *14*, R285−R340.

(55) Prozorov, R.; Prozorov, T.; Mallapragada, S. K.; Narasimhan, B.; Williams, T. J.; Bazylinski, D. A. Magnetic irreversibility and the Verwey transition in nanocrystalline bacterial magnetite. *Phys. Rev. B* **2007**, *76*, No. 054406.

(56) Fernandez, E.; Tu, K.-H.; Ho, P.; Ross, C. A. Thermal stability of L10-FePt nanodots patterned by self-assembled block copolymer lithography. *Nanotechnology* **2018**, *29*, No. 465301.

(57) Fischer, H.; Mastrogiacomo, G.; Loffler, J. F.; Warthmann, R. J.; Weidler, P. G.; Gehring, A. U. Ferromagnetic resonance and magnetic characteristics of intact magnetosome chains in *Magnetospirillum gryphiswaldense*. *Earth Planet. Sci. Lett.* **2008**, *270*, 200−208.

(58) Kronmüller, H.; Walz, F. Magnetic after-effects in $Fe_3 O_4$ and vacancy-doped magnetite. *Philos. Mag. B* **1980**, *42*, 433−452.

(59) Muxworthy, A. R.; McClelland, E. Review of the low-temperature magnetic properties of magnetite from a rock magnetic perspective. *Geophys. J. Int.* **2000**, *140*, 101−114.

(60) Stoner, E.; Wohlfarth, E. A mechanism of magnetic hysteresis in heterogenious alloys. *Philos. Trans. Royal Soc. A* **1948**, *240*, 599−642.

(61) Orue, I.; Marcano, L.; Bender, P.; García-Prieto, A.; Valencia, S.; Mawass, M. A.; Gil Carton, D.; Alba Venero, D.; Honecker, D.; García-Arribas, A.; et al. Configuration of the magnetosome chain: a natural magnetic nanoarchitecture. *Nanoscale* **2018**, *10*, 7407−7419.

(62) Huizar-Félix, A. M.; Muñoz, D.; Orue, I.; Magen, C.; Ibarra, A.; Barandiaran, J. M.; Muela, A.; Fdez-Gubieda, M. L. Assemblies of magnetite nanoparticles extracted from magnetotactic bacteria: A magnetic study. *Appl. Phys. Lett.* **2016**, *108*, No. 063109.

(63) Charilaou, M.; Kind, J.; García-Rubio, I.; Schüler, D.; Gehring, A. U. Magnetic anisotropy of non-interacting collinear nanocrystal-chains. *Appl. Phys. Lett.* **2014**, *104*, No. 112406.

(64) Charilaou, M.; Winklhofer, M.; Gehring, A. U. Simulation of ferromagnetic resonance spectra of linear chains of magnetite nanocrystals. *J. Appl. Phys.* **2011**, *109*, No. 093903.

(65) Gehring, A. U.; Fischer, H.; Charilaou, M.; García-Rubio, I. Magnetic anisotropy and Verwey transition of magnetosome chains in *Magnetospirillum gryphiswaldense*: Magnetic anisotropy and Verwey transition. *Geophys. J. Int.* **2011**, *187*, 1215−1221.

(66) Peddis, D.; Muscas, G.; Mathieu, R.; Kumar, P. A.; Varvaro, G.; Singh, G.; Orue, I.; Gil-Carton, D.; Marcano, L.; Muela, A.; et al. Studying nanoparticles' 3D shape by aspect maps: Determination of the morphology of bacterial magnetic nanoparticles. *Faraday Discuss.* **2016**, *191*, 177−188.

(67) Gandia, D.; Gandarias, L.; Marcano, L.; Orue, In.; Gil-Cartón, D.; Alonso, J.; García-Arribas, A.; Muela, A.; Fdez-Gubieda, M. Elucidating the role of shape anisotropy in faceted magnetic nanoparticles using biogenic magnetosomes as a model. *Nanoscale* **2020**, *12*, 16081−16090.

(68) Geoghegan, L. J.; Coffey, W. T.; Mulligan, B. Differential Recurrence Relations for Non-Axially Symmetric Rotational Fokker-Planck Equations. *Adv. Chem. Phys.* **1997**, *100*, 475−641.

(69) Carrey, J.; Mehdaoui, B.; Respaud, M. Simple models for dynamic hysteresis loop calculations of magnetic single-domain nanoparticles: Application to magnetic hyperthermia optimization. *J. Appl. Phys.* **2011**, *109*, No. 083921.

(70) Chikazumi, S. *Physics of Ferromagnetism 2e*; OUP Oxford, 2009.

(71) Penoyer, R. F.; Shafer, M. W. On the Magnetic Anisotropy in Manganese-Iron Spinels. *J. Appl. Phys.* **1959**, *30*, S315−S316.

(72) Alphandéry, E.; Ding, Y.; Ngo, A. T.; Wang, Z. L.; Wu, L. F.; Pileni, M. P. Assemblies of Aligned Magnetotactic Bacteria and Extracted Magnetosomes: What Is the Main Factor Responsible for the Magnetic Anisotropy. *ACS Nano* **2009**, *3*, 1539−1547.